

## Electron inelastic mean free path, electron attenuation length, and low-energy electron-diffraction theory

J. Rundgren\*

*Theory of Materials, Department of Physics, Royal Institute of Technology, SE-100 44 Stockholm, Sweden*

(Received 2 September 1998)

Low-energy electron diffraction (LEED) theory is used for describing the electron transport in crystalline solids with the purpose of determining the electron attenuation length. The inelastic scattering of the primary electron in the electron gas of the material is introduced into the LEED theory in terms of the electron inelastic mean free path derived by Tanuma, Powell, and Penn from the Lindhard dielectric function and optical data [Surf. Interface Anal. **17**, 911 (1991)]. The theorem of flux reversal for electrons in situations of inward and outward propagation is deduced from local inversion symmetry and specific boundary conditions at the sources. The theory is applied to 50–400 eV electrons incident on the three low-index surfaces of copper, and a fair agreement is found with a previous Monte Carlo simulation of the electron transport in amorphous copper. In addition to the inelastic electron-electron gas scattering, the inelastic electron-phonon scattering has a significant effect on the attenuation length in a crystalline material. The temperature parameter, necessary in a LEED calculation, does not occur in current Monte Carlo simulations. Common scattering potential models, at low energy, for LEED and for Auger electron spectroscopy and x-ray photoemission spectroscopy are discussed. [S0163-1829(99)03707-8]

### I. INTRODUCTION

The aim of the present paper is to compare Auger electron spectroscopy (AES) and x-ray photoemission spectroscopy (XPS) studies of electron emission depth at low energies with calculations of electron transmission in low-energy electron diffraction (LEED). The paper presents a dynamical LEED theory for the calculation of the electron attenuation length in crystalline solids, and the theory is applied to copper in the energy range 50–400 eV. The calculations are based on the tables of electron inelastic mean free path derived by Tanuma, Powell, and Penn (TPP) from the Lindhard dielectric function and optical data for 27 elemental solids.<sup>1,2</sup>

A fundamental interest in this comparison is that dynamical LEED is manifestly a multiple-scattering theory,<sup>3,4</sup> whereas current Monte Carlo simulations are based on the single-scattering Born approximation all the way from 2000 down to 50 eV.<sup>5</sup> An immediate question is whether Monte Carlo simulation is able to produce true emission depths in the low-energy regime.<sup>6,7</sup>

In a solid the primary intensity of electrons incident on the surface or created at internal sources is attenuated by the common effect of elastic and inelastic scattering. For electrons of keV primary energy the electron propagation follows a definite trajectory, and the elastic electron-ion core scattering can be described by the Born approximation. Because of the elastic collisions with ion cores the trajectory is not straight but zigzag, and the distance from a scattering node, where the electron preserves the primary energy to a point where an energy loss occurs, is always shorter than the inelastic mean free path  $\lambda_{\text{IMFP}}$ .

A LEED approach to the determination of electron transport attenuation is delineated in Sec. II. In ideal crystals the space-filling electron probability density is expandable in plane waves or beams, and the multiple electron scattering in

the lattice is calculated to infinite order by dynamical LEED theory.<sup>3,4</sup> Inelastic events are taken into account by means of an imaginary potential  $V_{0i}$ , often referred to as the absorptive or optical potential. More intensity is scattered out of the primary 00 beam into another  $hk$  beam than is backscattered from  $hk$  into 00 because of the inelastic losses occurring together with the elastic scattering events. Therefore, the spacing between a plane at depth  $z_1$ , where the electron has primary energy to a plane at  $z_2$  where it undergoes an energy loss, is generally less than  $\lambda_{\text{IMFP}}$ . In the following the average spacing  $|z_1 - z_2|$  is referred to as the attenuation length  $\lambda_{\text{AL}}$ .

Electron transport in LEED and in Monte Carlo simulation can be compared irrespective of the direction of propagation. Section III demonstrates that flux reversal follows from local inversion symmetry in the solid. Flux reversal is shown to be an asymptotic feature attained at such a great depth beyond the electron source that the intensity transients due to the particular boundary condition have levelled out.

The attenuation of the electron transport in a crystal is studied in great detail by LEED calculations on copper. In Sec. IV an elastic electron-ion core-scattering potential is designed, and the electron mean free path available in the TPP tables as a function of primary energy is transformed into an imaginary inner potential. The LEED spectra calculated for Cu(111) with these potentials excellently agree with the experimental data. The establishment of good scattering parameters for copper is an important prerequisite of the present note comparing the attenuation lengths calculated by LEED for crystalline copper and by Monte Carlo simulation for amorphous copper.

A series of case studies on the (111), (100), and (110) surfaces of copper in Sec. V show that the transmitted intensity decreases versus depth with a logarithmic gradient that is constant to a good approximation provided the primary beam

is incident at an angle less than about  $45^\circ$  from the surface normal. The attenuation lengths following from LEED are accompanied with orientational uncertainties due partly to interlayer propagators varying in magnitude with angle of incidence and partly to angular fine structure in the diffraction.

The fundamental concepts of LEED and Monte Carlo simulation are considered in Sec. VI in light of some previous review papers. The electron-copper scattering potential of the present paper is then discussed in relation to a particular differential scattering cross section used in the AES-XPS literature down to such low energy as 50 eV. It is remarked that the inelastic electron-phonon scattering is not considered in the current Monte Carlo simulations of electron transport. The author speculates whether temperature-dependent Monte Carlo simulation would confirm that an amorphous material has a similar forward electron-scattering lobe as a bare electron-ion core scatterer.

This paper on the attenuation length in copper ends in Sec. VII, the conclusion, by emphasizing the importance of the AES-XPS and LEED techniques applying equivalent models for elastic and inelastic scattering in their common energy range.

## II. ELECTRON TRANSMISSION

### A. LEED

Most LEED theories currently use the layer-doubling method for determining the wave field in the substrate and the reflection from the surface.<sup>3</sup> Given the reflection and the transmission at the two sides of a layer parallel to the surface, a LEED computer program calculates successively the reflection and transmission by one layer, two layers, four layers, and so forth. The layer-doubling converges when the imaginary inner potential  $V_{0i}$  is in the range 2.5–5 eV, which comprises most elements above 100 eV primary energy. The convergence is rapid like an exponential one, and three or four iterations are usually sufficient for structure determination. Layer-doubling still works, when the primary energy is very low and  $V_{0i}$  approaches 1 eV.

For primary energies greater than a few electron volts the backscattered LEED signal is weak compared with the incident electron intensity. This means that the magnitude of the wave field inside the surface is essentially determined by the forward-electron transmission. The transmission matrix of the  $i$ th layer-doubling iteration is denoted  $T_{\mathbf{g}\mathbf{g}'}^{(i)}$ , where  $\mathbf{g}$  stands for the Miller indices  $hk$  of a beam; the primary beam 00 is from now on denoted by a sole zero. Propagators leading from one atomic plane to another are included in  $T_{\mathbf{g}\mathbf{g}'}^{(i)}$ . The electron intensity carried by a beam  $\mathbf{g}$  through the stack of layers is expressed as flux in units of incident flux<sup>3</sup>

$$I_{\mathbf{g}}^{(i)} = \frac{|\operatorname{Re} k_{\mathbf{g}z}| |T_{\mathbf{g}0}^{(i)}|^2}{|\operatorname{Re} k_{0z}|} \quad (1)$$

where  $k_{\mathbf{g}z}$  is the  $z$  component of the wave vector  $k_{\mathbf{g}}$  of beam  $\mathbf{g}$ , and where  $i$  counts the iterations; the  $z$  direction is normal to the surface.

The decrease of beam intensities  $I_{\mathbf{g}}$  normal to the surface is conveniently visualized by diagrams of the logarithmic transmission gradient

$$L_{\mathbf{g}} = \frac{d \ln I_{\mathbf{g}}}{dz}. \quad (2)$$

Differential steps in  $z$  are not easily coded in the layer-doubling method, but  $L_{\mathbf{g}}$  can be set up as

$$L_{\mathbf{g}}^{(i)} = \frac{\ln I_{\mathbf{g}}^{(i)}}{z^{(i)}} \quad (3)$$

because the attenuation length is defined from a transmission intensity that decreases exponentially, in which situation  $L_{\mathbf{g}}$  and  $L_{\mathbf{g}}^{(i)}$  above are constant and equal. The logarithmic transmission gradient is known in the AES-XPS literature under the name of ‘‘emission depth distribution function.’’<sup>8–10</sup>

Case studies of  $L_{\mathbf{g}}^{(i)}$  made in the energy range 20–400 eV show that a strong exchange of intensity can occur between the primary beam and the other beams and that  $I_0^{(i)}$  can exhibit the typical behavior of the *Pendellösung* or pendulum solution of Ewald in electron transmission microscopy.<sup>11</sup> The outermost layers of the crystal generate the backscattering from the surface, and, correspondingly, one sees a transient in  $L^{(i)}$  during the iterations  $i \leq 3$ , where a depth  $z^{(i)}$  of less or equal to eight layers is attained. In other words, the boundary condition at the surface influences the wave solution to the Schrödinger equation down to  $z^{(3)}$ . This view on the wave field is further discussed in Secs. III and V.

The total intensity of all the beams

$$I^{(i)} = \sum_{\mathbf{g}} I_{\mathbf{g}}^{(i)} \quad (4)$$

has a logarithmic gradient  $L^{(i)}$ , which varies relatively slowly with depth because of cancellations among the beam-intensity exchanges. At greater depth  $i > 3$ , where the backscattering transient has vanished,  $L^{(i)}$  generally tends to a constant value ( $< 0$ ) provided that the off-normal incidence angle is less than about  $45^\circ$ . Outside the  $45^\circ$  admission cone  $L^{(i)}$  slowly increases with  $i$ . A logarithmic transmission gradient  $L^{(i)}$  that is constant with respect to  $i$  corresponds to an exponentially decreasing intensity proportional to  $\exp(L^{(i)}z)$ , whereas a slowly increasing gradient can be described as a ‘‘stretched’’ exponential decrease like  $\exp(az^\beta)$  ( $a < 0$  and  $0 < \beta < 1$ ).

The logarithmic transmission gradient  $L^{(i)}$  corresponding to exponential intensity decrease in the admission cone of semiangle  $45^\circ$  defines an attenuation length

$$\lambda_{\text{AL}} = -\frac{1}{L^{(i)}} \quad (i \geq 3). \quad (5)$$

From the qualitative arguments presented in Sec. I one infers that  $\lambda_{\text{AL}} < \lambda_{\text{IMFP}}$  for the joint effect of inelastic and elastic scattering. At very low energy, where the wavelength of the primary electron is unable to resolve the crystal structure and only the specular beam is backscattered, it is expected that  $\lambda_{\text{AL}}$  approaches  $\lambda_{\text{IMFP}}$ .

### B. Inelastic mean free path

When the atomic graininess of a solid is disregarded, a primary electron propagates in any direction  $z$  as a plane

wave  $\psi = \exp(ikz)$ , undisturbed by diffraction but attenuated by inelastic scattering, hence with a wave number  $k$  that is complex. The intensity of the wave then decreases with a factor  $1/e$  over the inelastic mean free path  $\lambda_{\text{IMFP}}$ ,

$$\lambda_{\text{IMFP}} = \frac{1}{2 \text{Im } k}. \quad (6)$$

The motion of the primary electron of energy  $E$  in the homogeneous electron gas is governed by the energy-momentum relation  $E = \frac{1}{2}k^2 + V_0$ , where  $V_0 = V_{0r} + iV_{0i}$  is a complex potential composed of the real inner potential  $V_{0r}$  ( $<0$ ) and the imaginary optical potential  $V_{0i}$  ( $<0$ ). Atomic units are used and the energy scale is referred to the Fermi energy. The energy-momentum relation gives the following connection between the the electron absorption quantities for propagating waves ( $E - V_{0r} > 0$ ),

$$2V_{0i}\lambda_{\text{IMFP}} = V_{0i}(\text{Im } k)^{-1} = -\{2(E - V_{0r}) + (2\lambda_{\text{IMFP}})^{-2}\}^{1/2} \quad (7)$$

$$= -\{E - V_{0r} + [(E - V_{0r})^2 + V_{0i}^2]^{1/2}\}^{1/2}. \quad (8)$$

The homogeneous electron-gas model provides an imaginary potential  $V_{0i}$  through Eq. (7). The energy dependence of  $\lambda_{\text{IMFP}}$  is known for 27 elements by TPP's tables based on optical data,<sup>2</sup> and the energy dependence of  $V_{0r}$  can be derived from the interstitial charge density of the solid by the local density approximation. When used in LEED,  $V_{0i}(E)$  describes the electron absorption in a solid to a good approximation (Sec. IV).

In crystals the electron field has translational periodicity parallel to the surface, and electron losses can only occur in wave motion in the  $z$  direction perpendicular to the surface. The separated  $z$  directed motion of an electron in beam  $\mathbf{g}$  has a complex wave-vector component  $k_{gz}$  and an energy of propagation

$$E_{gz} = E - \frac{1}{2}|\mathbf{k}_{\parallel} + \mathbf{g}|^2, \quad (9)$$

when the primary beam is incident with a wave-vector component  $\mathbf{k}_{\parallel}$  parallel to the surface. Equation (8) determines  $\text{Im } k_{gz}$  on replacement of  $k$  by  $k_{gz}$  and of  $E$  by  $E_{gz}$ .

The stretched exponential intensity decrease occurring at near-to-grazing incidence is a feature of the interlayer propagators  $\exp(ik_{gz}d)$  ( $d$  is the interlayer spacing). Figure 1 illustrates the interlayer propagator by its magnitude  $\exp(-d \text{Im } k_{gz})$  regarded as a function of the variable  $q = \frac{1}{2}|\mathbf{k}_{\parallel} + \mathbf{g}|^2/E$ , which is the energy of propagation parallel to the surface expressed in units of the primary energy  $E$ . In particular, for the specular beam the  $q$  variable equals  $\sin^2\theta$ , where  $\theta$  is the angle of incidence. The diagram in Fig. 1 is drawn for the Cu(111) surface with consideration of the energy dependence of  $V_{0r}$  and  $V_{0i}$ . It turns out that the interlayer propagator begins a substantial decrease beyond  $q = 0.5 - 0.75$ , corresponding to an off-normal incidence of  $45^\circ - 60^\circ$  for the specular beam.  $\text{Im } k_{gz}$  assumes its minimum value with the least wave number  $|\mathbf{k}_{\parallel} + \mathbf{g}|$  of surface parallel propagation and the greatest energy  $E_{gz}$  available for propagation normal to the surface. When the primary incidence is close to the surface normal, the primary intensity

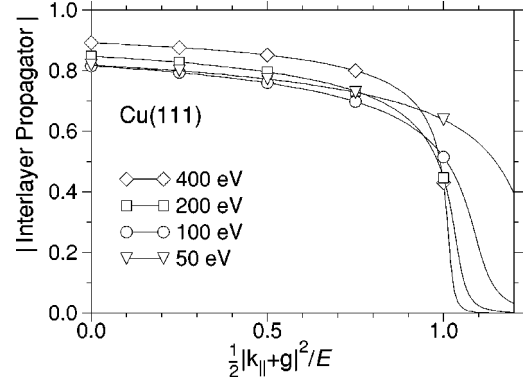


FIG. 1. The absolute value of interlayer propagators in Cu(111) drawn vs  $\frac{1}{2}|\mathbf{k}_{\parallel} + \mathbf{g}|^2/E$ , the energy of propagation parallel to the surface in units of the primary energy  $E$ .

has minimum attenuation and predominates at all depths. On the other hand, a primary beam approaching grazing incidence undergoes a relatively strong attenuation. The elastic scattering then gradually transmits primary electron flux towards beams having  $|\mathbf{k}_{\parallel} + \mathbf{g}| < |\mathbf{k}_{\parallel}|$  and attenuation similar to that of perpendicular motion. In the latter case, therefore, the negative logarithmic gradient  $L^{(i)}$  slowly increases with depth. LEED calculations on low-index copper surfaces indicate that the angle of incidence distinguishing exponential decrease from stretched exponential decrease is roughly  $45^\circ$ .

### III. FLUX REVERSAL

LEED electrons propagate from the surface and inwards, while AES and XPS electrons emerge from internal sources. This section demonstrates that the electron transport in solids is reversible in the sense that the flux is the same function of distance in the inward and outward direction provided two conditions are fulfilled. The crystal structure has to have local inversion symmetry, and the flux has to be considered at distances beyond the extension of the transient generated by the boundary condition at the source.

In the solid occupying half-space  $z > 0$  the electron transport is governed by the Schrödinger equation and a continuity equation with a sink. The sink is assumed to be a uniformly distributed absorptive potential  $V_{0i}$  ( $<0$ ), and the elastic scattering is described by a potential  $V_r(x, y, z)$  with nuclear singularities corresponding to the periodic or amorphous atomic structure. The Schrödinger equation with a complex scattering potential

$$V(x, y, z) = V_r(x, y, z) + iV_{0i} \quad (10)$$

determines a complete set of linearly independent basis functions. These are conveniently arranged in two sets of functions  $\phi_n(x, y, z)$  and  $\phi_{-n}(x, y, z)$  ( $n = 1, 2, \dots$ ), whose fluxes decrease in the positive and negative  $z$  direction, respectively. Let  $n = 1$  correspond to minimum decrease.

If the elastic scattering potential has local inversion symmetry at a plane  $z = z_0$ ,

$$V_r(x, y, z) = V_r(x, y, 2z_0 - z) \quad (11)$$

the basis functions will obey the symmetry relation

$$\phi_{-n}(x, y, z) = \text{const} \times \phi_n(x, y, 2z_0 - z). \quad (12)$$

Then, in the vicinity of  $z=z_0$ , the fluxes of  $\phi_n$  and of  $\phi_{-n}$  decrease in opposite  $z$  directions with logarithmic gradients of equal magnitude. Consider now two electron transport situations, one electron wave generated by a source at the surface and propagating inwards

$$\psi_{\text{inw}} = \sum_n A_n \phi_n \quad (13)$$

and another electron wave driven by a source in the interior of the crystal and propagating outwards

$$\psi_{\text{outw}} = \sum_n B_n \phi_{-n}. \quad (14)$$

$A_n$  and  $B_n$  are excitation coefficients determined by an external and an internal boundary condition, respectively. Electron transport is reversible,

$$\psi_{\text{outw}}(x, y, z) = \text{const} \times \psi_{\text{inw}}(x, y, 2z_0 - z), \quad (15)$$

provided the boundary conditions at the surface or at an internal source are the same. In general they are different, and the waves  $\psi_{\text{inw}}$  and  $\psi_{\text{outw}}$  do not exhibit strict inversion symmetry. However, on the assumption that the source gives rise to a beam spectrum containing a primary wave  $\phi_1$  of predominant intensity, the elastic scattering lobes of the atoms, large for the forward scattering, will generate an asymptotic electron wave that is specific to the material. In the presence of local inversion (11) such asymptotic electron transport is reversible.

Cubic crystals have inversion symmetry. The LEED study on copper in Sec. V shows that asymptotic transmission is attained upon three layer doublings.

In an amorphous material inversion symmetry is everywhere present to a good approximation, and flux reversal holds in the nontransient region. The concept of trajectory (or flux) reversal was introduced by Gries and Werner in connection with electron transport in AES and XPS.<sup>9</sup> Later the flux transients occurring in the vicinity of the boundary at a surface or an interface were extensively studied by Monte Carlo simulations.<sup>12</sup>

In crystals where inversion symmetry of type (11) does not occur, the logarithmic gradients are expected to depend significantly on the direction of electron transport. An idea about such a directional effect can perhaps be gained by considering the electric resistivity of noncubic metals.<sup>13</sup> For instance, the resistivities of Be, Sn, and Zn have the parallel-to-perpendicular ratios 1.2, 1.4, and 1.03, respectively.

#### IV. LEED ON COPPER

The theory presented in the previous sections will be illustrated by LEED calculations on the three low-index surfaces of copper, which were earlier subject to extensive LEED studies, namely Cu(111),<sup>14</sup> Cu(100),<sup>15-17</sup> and Cu(110).<sup>17-20</sup> The experimental LEED data on Cu(111), which are available to the author, will be used for establishing an appropriate LEED scattering potential for copper.

#### A. Elastic and inelastic scattering

An elastic scattering potential for copper in a fcc lattice is calculated by the superposition of atomic charge densities<sup>21</sup> generated by a self-consistent-charge Hartree-Fock-Slater code.<sup>22-24</sup> This code has both a nonrelativistic and a relativistic option, of which the former is sufficient in the present context. Afterwards an excited-state potential  $V_{\text{xc}}(E)$  describing the exchange and correlation energy of the primary electron is designed by means of the Hedin-Lundqvist local density approximation.<sup>25-27</sup>

The *ad hoc* multiplicative factor to  $V_{\text{xc}}(E)$  introduced by Hedin and Lundqvist in their theory is conveniently used for adjustment of the local density approximation to the nonuniform charge density in a crystal. In the case of Cu(111), the factor 0.96 brings the peaks of the theoretical and experimental spectra into excellent agreement. The result is the following energy-dependent inner potential for copper

$$V_{\text{or}}(E) = \max[-13.4, -3.6 - 65.8(E + 10.0)^{-1/2}] \quad (16)$$

as referred to the vacuum level. The ground-state inner potential  $-13.4$  eV is valid up to  $E \approx 36$  eV, where the excited-state inner potential takes over. In expression (16) the work function is assumed to be 4 eV, but in the later LEED calculations  $V_{\text{or}}(E)$  is adjusted to the energy scale of the experiment by a constant shift.

The partial-wave phase shifts  $\delta_l(E)$  ( $l$  is the orbital quantum number) calculated from the present electron-ion core potential<sup>28</sup> nicely follow the rule of thumb that the number of phase shifts scales as  $E^{1/2}$  for a given accuracy:  $\delta_l(100 \text{ eV}) \leq 0.002$  for  $l \geq 7$ , and  $\delta_l(400 \text{ eV}) \leq 0.003$  for  $l \geq 12$ .

The effect on LEED from inelastic electron-phonon scattering due to the thermal vibrations of the crystal lattice can be taken into account in the calculations by a Debye-temperature dependent real-to-complex transformation of the phase shifts.<sup>3</sup> The Cu(111) data were recorded at an ambient temperature of 300 K, and it turns out that the listed Debye temperature for copper, 315 K,<sup>29</sup> is perfect for the calculation of the Cu(111) spectra. The vibrational enhancement in the topmost layer is expected to be very small due to the denseness of the layer and is not detectable with the limited amount of data available on Cu(111).

An imaginary inner potential  $V_{\text{oi}}(E)$  follows through Eq. (7) from TPP's calculation of the inelastic mean free path (Ref. 2, Table II, and Ref. 5, Table I). These tables extend from 50 eV and upwards, while the LEED data on Cu(111) (Ref. 14) go down to very low energy. For the purpose of comparing the present LEED calculation on Cu(111) with the previously published structure determination, the author takes the liberty to extrapolate the  $V_{\text{oi}}(E)$  curve following from the TPP calculation down to 20 eV with proper attention to the intensity of the low-energy peaks in the specular-beam spectrum.  $\lambda_{\text{IMFP}}$  and  $V_{\text{oi}}$  for copper are drawn as functions of energy in Fig. 2.

#### B. LEED spectra and $r$ -factor

The analysis of electron transmission inside the low-index surfaces of copper is carried out using the computer code of Rundgren and Salwén,<sup>30</sup> which contains layer-doubling rou-

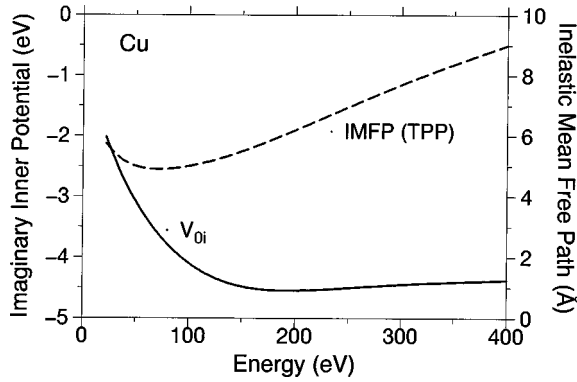


FIG. 2. Inelastic mean free path and imaginary inner potential for copper.

tines easily adaptable to the operations in Sec. II. The numerics of the code was carefully tested against the LEED program of Moritz and co-workers.<sup>31,32</sup> The LEED spectra for Cu(111) are illustrated in Fig. 3.

As  $r$  (reliability) factor for estimating the misfit between theory and experiment this paper uses the metric distance<sup>33,14</sup>

$$D_1 = \frac{1}{2} \sum_{\mathbf{g}} \int |I_{\mathbf{g},\text{th}} - I_{\mathbf{g},\text{ex}}| dE, \quad (17)$$

where the theoretical and experimental spectra,  $I_{\mathbf{g},\text{th}}$  and  $I_{\mathbf{g},\text{ex}}$ , respectively, are normalized to unit integral over the energy range of beam  $\mathbf{g}$ . The spectra in Fig. 3 give a  $D_1$  value equal to 9% like in the original structure determination of Cu(111).<sup>14</sup> Visual inspection of the diagrams in the previous and the present paper gives a slight preference to the agreement obtained in the latter, in particular, regarding the specular beam.

The peaks in  $I_{\mathbf{g},\text{th}}$  and  $I_{\mathbf{g},\text{ex}}$  are well positioned in relation to each other, which directly shows that the energy dependence of  $V_{0i}$  is correct to a good approximation.

$I_{\mathbf{g},\text{th}}$  and  $I_{\mathbf{g},\text{ex}}$  have virtually equal peak widths, which determine  $V_{0i}$  as a function of energy. In addition, it is interesting to consider the magnitude of the theoretical and experimental spectra *before* the beamwise normalization on the assumption that the experimental beam spectra are referred to the same incident intensity. Consulting the raw data of the LEED experiment, one finds (in arbitrary units) the ratio 1.5

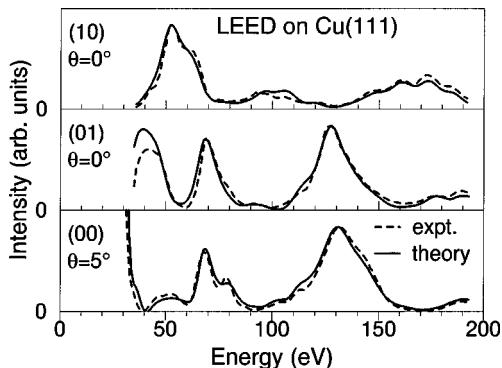


FIG. 3. LEED study of Cu(111) with experimental data from Lindgren *et al.* (Ref. 14). Individual intensity scalings make the theoretical and experimental spectra coalesce, for presentation purpose.

for the 131 eV peak in the 00 spectrum, the ratio 1.4 for the 173 eV peak in the 10 spectrum, and the ratio 1.4 for the 128 eV peak in the 01 spectrum. The magnitudes are convincingly coherent.

It is noted that the excellent agreement of theory and experiment shown in Fig. 3 is achieved without any optimization of the inelastic input parameters, which are the Debye temperature and the imaginary inner potential derived from TPPS's  $\lambda_{\text{IMFP}}$  table.

The inelastic electron-phonon scattering has an important effect on the intensity and shape of the LEED spectra. When the temperature is put equal to 0 K instead of 300 K in the LEED calculation on Cu(111), the metric distance  $D_1$  jumps from 9% to 14%, which indicates a significant LEED sensitivity to temperature.

## V. ATTENUATION IN COPPER

### A. Logarithmic transmission gradient

The attenuation of the electron field in the crystal is obtained from the total transmitted intensity  $I^{(i)}$  as a function of the depth of penetration  $z^{(i)}$ . Figure 4 conveys a general idea about the attenuation of the electron field by diagrams of the logarithmic transmission gradient versus depth for the Cu(111) surface at the angles of incidence  $\theta = 10^\circ, 45^\circ$ , and  $60^\circ$ . As expected from the angular dependence of the inter-layer propagators illustrated in Fig. 1, one finds that the logarithmic transmission gradient is virtually constant for  $10^\circ$ , roughly constant up to  $45^\circ$ , and substantially increasing for  $60^\circ$ . In the present paper the logarithmic gradient is taken to be the value at the sixteenth layer for all incidence angles.

### B. Attenuation length

The present paper reports LEED calculations on the (111), (100), and (110) surfaces of copper for incidence angles 0–70 degrees in steps of 5 degrees. The attenuation length, which is the reciprocal logarithmic transmission gradient, [Eq. (5)] will now be studied as a function of the incidence coordinates: primary energy  $E$ , off-normal angle  $\theta$ , and azimuth  $\phi$ . In addition, the attenuation length depends on the surface index. In Figs. 5–7 the attenuation lengths for copper calculated by LEED are compared with the values obtained by Cumpson and Seah (CS) using Monte Carlo simulation.<sup>5</sup>

Figure 5 shows  $\lambda_{\text{AL}}$  as a function of primary energy for the Cu(111) surface. With a fixed azimuth two incidences are chosen, one at  $10^\circ$  and one at the side of the  $45^\circ$  admission cone. The seemingly irregular structure in the  $\lambda_{\text{AL}}(E)$  curve is caused by numerous constructive and destructive interferences occurring in the elastic electron scattering.

Figure 6 represents  $\lambda_{\text{AL}}$  as a function of the off-normal incidence and primary energy for the three low-index surfaces of copper. The curves show the same general trends in all three cases. Although locally they vary differently, the curves attain roughly the same height at each particular energy. The minimum value of  $\lambda_{\text{AL}}$  occurs for primary energies around 100 eV.

Figure 7, finally, illustrates the dependence of  $\lambda_{\text{AL}}$  on azimuthal angle and primary energy for  $20^\circ$  off-normal incidence at the Cu(111) surface. Again, the intensity shows a vivid diffractive structure.

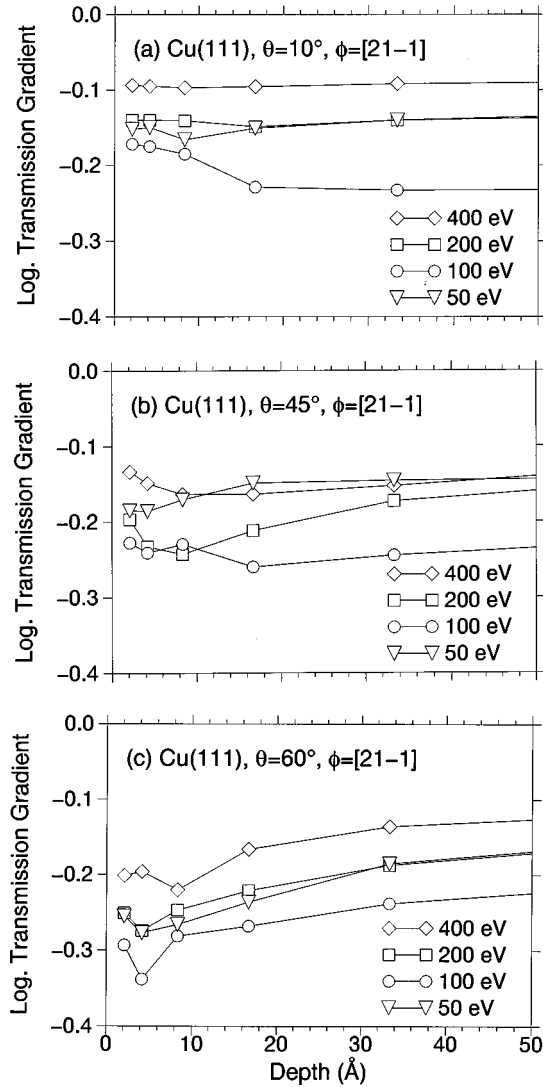


FIG. 4. Logarithmic transmission gradient at the Cu(111) surface. Azimuth is  $[21\bar{1}]$ , and angle of incidence is (a)  $10^\circ$ , (b)  $45^\circ$ , and (c)  $60^\circ$ .

### C. Orientational uncertainty

A comprehensive description of the electron transmission as a function of primary energy is obtained by calculating the average attenuation length in the  $45^\circ$  admission cone, where the transmitted intensity decreases exponentially. The pertaining standard deviation estimates the orientational variation of the attenuation length. The present calculation, applied separately to the three low-index surfaces of copper, is carried out using the grids  $\theta=0^\circ-45^\circ$  in steps of  $5^\circ$  and  $\phi=0^\circ-345^\circ$  in steps of  $15^\circ$  of which the latter grid is reducible by the particular surface symmetry. The surface-specific results are listed in Table I, and a global average with standard deviation is illustrated in Fig. 8 for the energy range 50–400 eV. The calculations are carried out both at 0 and 300 K to illustrate that the attenuation length in crystalline materials is sensitive to temperature. The gap between the 0 K curve and the 300 K curve turns out to increase with increasing energy and attains  $0.8 \text{ \AA}$  at 400 eV. For comparison with the Monte Carlo simulation method, Table I contains the attenuation length for copper calculated by CS.<sup>5</sup>

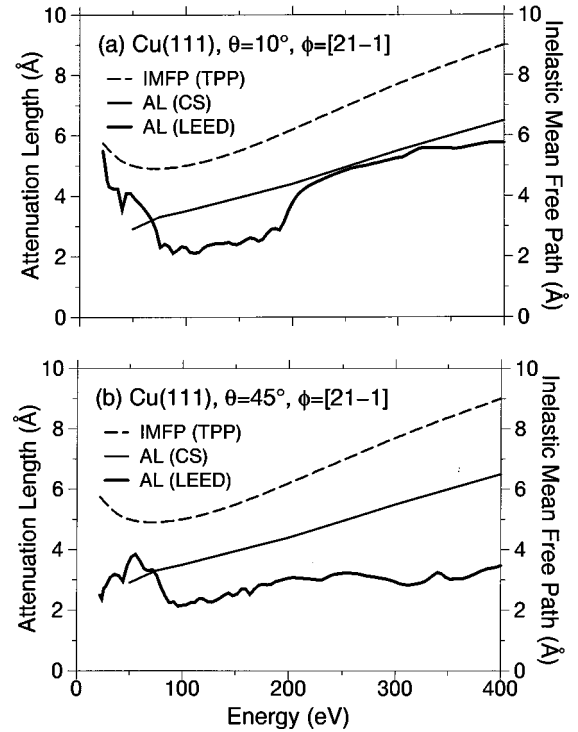


FIG. 5. Inelastic mean free path and attenuation length in Cu(111). Azimuth is  $[21\bar{1}]$ , and angle of incidence is (a)  $10^\circ$ , and (b)  $45^\circ$ .

It is noted that the uncertainties given in Table I and plotted in Fig. 8 are, in fact, not error bars caused by any numerical approximation but are due to the orientational variation of the diffraction. The dispersion of the attenuation length belonging to a particular crystal face amounts to  $0.2-0.4 \text{ \AA}$ . A polycrystalline copper sample, which exhibits several surface faces, can have larger dispersion.

## VI. DISCUSSION

Starting from LEED theory one is naturally led to the concept of “logarithmic transmission gradient,”  $L = (d/dz) \ln I$ , for describing the decrease of the electron flux and for defining an attenuation length. The concept of “emission depth distribution” used in AES-XPS literature is defined by the same derivative of the intensity as above, but the naming used in this note was preferred because of its allusion to transmission matrix, which is a corner stone of LEED theory.<sup>3</sup>

### A. LEED and Monte Carlo simulation

In Sec. V the attenuation length in copper is calculated from the nontransient part of the electron transmission with neglect of the boundary condition at the surface. Current Monte Carlo simulations utilize nontransience in the same way.<sup>9,5</sup> But the two descriptions of electron transmission go apart already from Eq. (7). LEED theory uses  $V_{0i}$  and Monte Carlo simulation  $\lambda_{\text{IMFP}}$ . The imaginary potential gives rise to a continuity equation for the electron probability density with a sink, giving a continuous probability for electron absorption. In the Monte Carlo simulation with inelastic mean

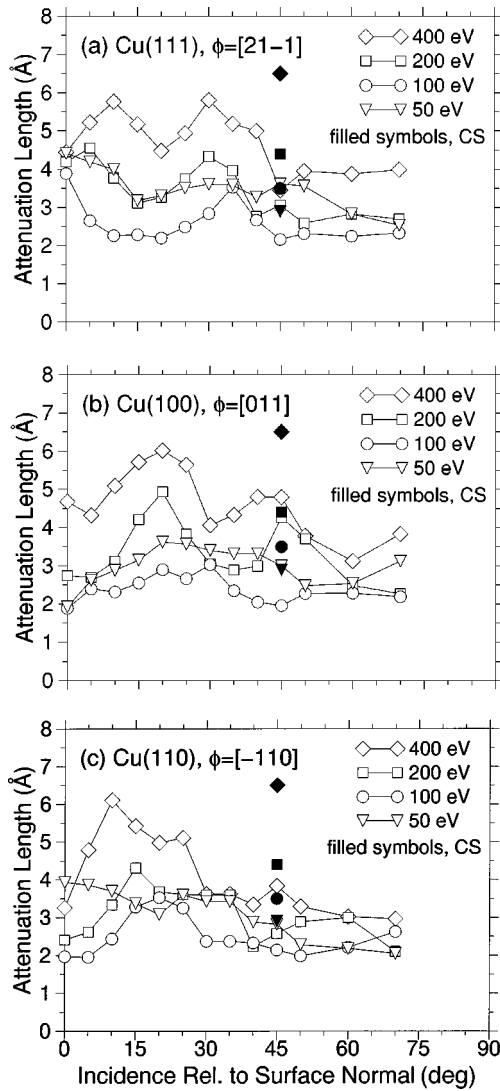


FIG. 6. Attenuation length as a function of off-normal incidence and primary energy for three low-index surfaces of copper (a) Cu(111), (b) Cu(100), and (c) Cu(110). Comparison with a Monte Carlo simulation (CS) (Ref. 5).

free path, the electron trajectory is a pearl-rope of elastically scattering ion cores, sooner or later broken off by an inelastic event.

The low-energy limit, below which the single-scattering Born approximation is unjustified with a given standard of accuracy, is not known.<sup>7</sup> Generalizations of the methods dedicated to either amorphous or crystalline materials have

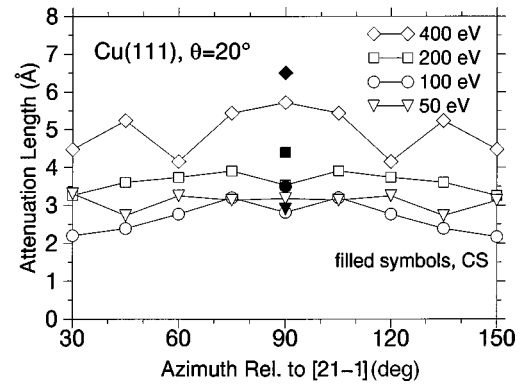


FIG. 7. Attenuation length as a function of azimuth and primary energy for Cu(111). Comparison with a Monte Carlo simulation (CS) (Ref. 5).

been discussed quite a long time from the points of view of AES-XPS (Refs. 6,7) and LEED.<sup>34</sup> Diffuse LEED treats amorphousness in an atomic layer adsorbed on a crystal by a cluster calculation. The cluster size is limited by the inelastic events which prevent electrons at a given point to feel atomic structure at a distance.<sup>35</sup>

It was hoped that the present LEED calculation and the Monte Carlo simulation on copper would converge near the upper-energy limit of 400 eV. No such tendency is seen in Fig. 8. The LEED and CS curves run more or less parallel above 100 eV.

A major difference between the calculations of CS and the present paper is that the former are applied to an amorphous material, whereas the latter are carried out on a crystal. Disorder by itself causes incoherence and electron absorption in diffraction, as, for instance, in the case of random metallic alloys.<sup>36</sup> If a disorder argument is important in the present context, the electron absorption in an amorphous material would be stronger than in a crystalline one. In Fig. 8 the attenuation length of CS is in fact longer than the LEED one both at 0 K and at 300 K. The intensity is further discussed in the following two subsections.

The LEED attenuation lengths presented in Table I and Fig. 8 are subject to orientational uncertainty caused by two effects. First, the intensity variation due to the angular dependence of the interlayer propagators (Sec. II B), and, second, the diffractive intensity variations with respect to  $E$ ,  $\theta$ ,  $\phi$ , and crystal face (Sec. V B). These orientational uncertainties add up to 10–15%. CS demonstrate that the attenuation length given by Monte Carlo simulation is a smooth function of emission angle  $\theta$ . The authors estimate

TABLE I. Attenuation length (in Å) vs energy for three low-index surfaces of copper.

$E$ (eV)	at 300 K				at 0 K		CS (Ref. 5)
	(111)	(100)	(110)	(111)	(100)	(110)	
50	$3.3 \pm 0.5$	$2.9 \pm 0.5$	$3.3 \pm 0.4$	$3.4 \pm 0.6$	$3.1 \pm 0.4$	$3.5 \pm 0.4$	2.9
75	$3.0 \pm 0.5$	$2.7 \pm 0.4$	$2.7 \pm 0.4$	$3.1 \pm 0.5$	$2.9 \pm 0.5$	$2.8 \pm 0.5$	3.3
100	$2.7 \pm 0.5$	$2.5 \pm 0.4$	$2.6 \pm 0.5$	$2.9 \pm 0.5$	$2.7 \pm 0.5$	$2.7 \pm 0.5$	3.5
200	$3.6 \pm 0.5$	$3.3 \pm 0.5$	$3.2 \pm 0.6$	$4.0 \pm 0.6$	$3.6 \pm 0.6$	$3.7 \pm 0.5$	4.4
300	$4.4 \pm 0.6$	$4.2 \pm 0.7$	$4.0 \pm 0.8$	$4.9 \pm 0.7$	$4.7 \pm 0.7$	$4.5 \pm 0.8$	5.5
400	$5.0 \pm 0.7$	$4.9 \pm 0.7$	$4.8 \pm 0.9$	$5.6 \pm 0.9$	$5.7 \pm 0.7$	$5.4 \pm 0.9$	6.5

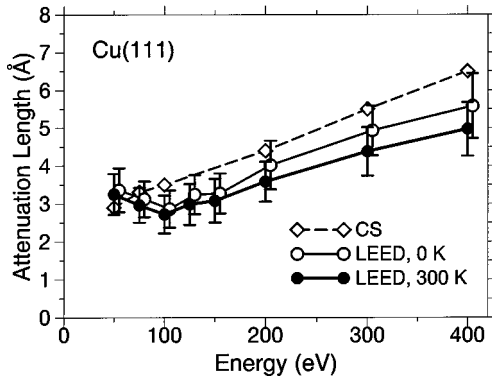


FIG. 8. Attenuation length for Cu(111) in a  $45^\circ$  admission cone about the surface normal; comparison with a Monte Carlo simulation (CS) (Ref. 5). Vertical bars show orientational uncertainties; the middle curve is shifted 5 eV to the right for clarity.

the “maximum usable emission angle” for a given accuracy of emission depth and find that 5% accuracy defines a  $58^\circ$  admission cone.<sup>5</sup>

### B. Elastic scattering

A basic element in the calculation of electron attenuation lengths is the elastic electron-ion core scattering potential. In their Monte Carlo simulation CS use the differential scattering cross section tabulated as a function of energy by Czyzewski *et al.*<sup>37</sup> If the pertaining electron-scattering phase shifts had been available, the immediate action had been to apply them to a LEED calculation. Instead, the differential scattering cross section will be used to shed some light on the attenuation lengths illustrated in Fig. 8.

Figure 9 shows the differential cross section for copper at 100 eV following from the superposition of Hartree-Fock-Slater charge densities in Sec. IV A together with the differential cross section produced by the relativistic Hartree-Fock method of Czyzewski *et al.* In the first place the 0 K curve of the present paper is considered. One finds a substantial discrepancy between the cross sections of the two papers, of which the latter is said to have little experimental support below 1 keV.<sup>37</sup> The electron-scattering potential generated in Sec. IV A reproduces extremely well the LEED spectra on Cu(111) as demonstrated in Fig. 3 and is considered the pre-

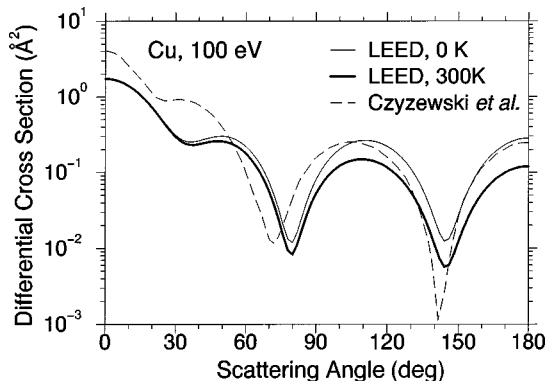


FIG. 9. Differential scattering cross section for copper at 100 eV from a self-consistent-charge Hartree-Fock-Slater model applied to a fcc lattice of ion cores; comparison with the Hartree-Fock calculation of Czyzewski *et al.* (Ref. 37).

TABLE II. Imaginary potential  $V_{0i}$  for copper from selected LEED works.

Surface	$V_{0i}$ (eV) with Refs.
(111)-(1 $\times$ 1)	-4.6 (Ref. 14)
(100)-(1 $\times$ 1)	-4 (Ref. 15–17)
(110)-(1 $\times$ 1)	$-2.5 \pm 0.3$ (Ref. 18), -4 (Refs. 17 and 19)
(110)-(1 $\times$ 2)	-5 (Ref. 20)

ferred one. The fact that the electron-scattering potential of Czyzewski *et al.* overestimates the forward scattering, may explain that the CS calculation gives greater attenuation length than the LEED calculation.

### C. Inelastic scattering

The attenuation length depends on temperature in LEED theory as shown in Fig. 8, while temperature does not occur as a parameter in current Monte Carlo simulations.

Figure 9 shows how the inelastic electron-phonon scattering due to lattice vibrations influences the effective differential-scattering cross section of the ion cores. The sensitivity to temperature varies from nothing in the forward direction to a maximum in the backward direction. In the case of 100 eV primary energy the backscattered intensity relative to the forwardscattered intensity is 0.16 at 0 K and 0.07 at 300 K; at 400 eV the corresponding ratios are 0.07 and 0.003. Although the backscattering is thus found rapidly to decrease in relative intensity when the energy increases, the LEED calculation illustrated in Fig. 8 shows that the effect of thermal motion on the attenuation length is strong and roughly the same in the whole energy range 50–400 eV. In crystalline materials mirror planes give rise to multiple scattering, which can amplify backward scattering and the effect of thermal motion.

A hypothesis close at hand is that amorphous materials, where there is no analogue to multiple scattering between mirror planes, scatter electrons in the forward direction much like the ion cores. Monte Carlo simulation with temperature-dependent differential scattering cross sections would then show a very weak effect on the attenuation length, and the single-scattering Born approximation could be valid down to some low energy. A test calculation to see whether the effect of lattice vibrations is observable with the current resolution of AES-XPS equipments is beyond the scope of the present paper.

The agreement of theoretical and experimental LEED spectra for copper shown in Fig. 3 is achieved without any optimization of the inelastic-input parameters, which are the Debye temperature and the imaginary inner potential  $V_{0i}$  derived from TPP’s  $\lambda_{\text{IMFP}}$  table.  $V_{0i}$  illustrated in Fig. 2 is approximately constant in a large energy interval; it assumes its minimum value  $-4.54$  eV at about 200 eV primary energy and increases to  $-4.37$  eV at the primary energies 128 and 400 eV.

The imaginary inner potentials determined in eight LEED investigations on copper are presented in Table II. Reference is made to works which use a  $V_{0i}(E)$  that remains constant or has a minimum<sup>14</sup> like in Fig. 2. The heuristic  $-E^{1/3}$  model is left out of consideration, because it is de-

creasing at high energy. Table II gives a mean imaginary inner potential  $-4.0$  eV, accompanied with an important root mean-square dispersion,  $0.7$  eV. The mean LEED value roughly agrees with the TPP value for copper,  $-4.4$  eV in the range  $128$ – $400$  eV, but the LEED technique is probably capable of less dispersion in  $V_{0i}$  than the above.

## VII. CONCLUSION

Flux reversal for electron transport in crystals and amorphous materials is derived from local inversion symmetry. The flux reversal is limited to the region exterior to the wave-field transients due to the boundary conditions at the source and at interfaces.

This paper is a comparison between attenuation lengths calculated by LEED and by Monte Carlo simulation. A fair agreement is found for crystalline and amorphous copper. Details concerning the scattering parameters remain to be clarified before the low-energy limit of the Born approximation to electron transmission can be determined.

It is of general physical interest that AES-XPS and LEED utilize compatible electron-ion scattering potentials, where the energy regions of the methods overlap. LEED establishes valid potentials for elements at energies extending to some  $500$  eV. A great body of experimental evidence exists; in 1995 the LEED literature contained 156 surface studies on clean metals and semiconductors distributed on 31 elements.<sup>38</sup>

TPP's table of inelastic mean free paths for 27 elements<sup>2</sup> establishes a standard for the design of imaginary inner potentials for LEED. The negative  $V_{0i}$ 's following from the  $\lambda_{\text{IMFP}}$ 's through Eq. (7) are all found to go through a minimum somewhere in the interval  $100$ – $300$  eV and slowly to increase towards high primary energy.

## ACKNOWLEDGMENT

The author wishes to thank M. P. Seah for a helpful communication.

\*Electronic address: jru@theophys.kth.se

<sup>1</sup>S. Tanuma, C.J. Powell, and D.R. Penn, *Surf. Interface Anal.* **11**, 577 (1988).

<sup>2</sup>S. Tanuma, C.J. Powell, and D.R. Penn, *Surf. Interface Anal.* **17**, 911 (1991).

<sup>3</sup>J. B. Pendry, *Low-Energy Electron Diffraction* (Academic, London, 1974).

<sup>4</sup>M. A. Van Hove, W. H. Weinberg, and C. M. Chan, *Low-Energy Electron Diffraction* (Springer, Berlin, 1986).

<sup>5</sup>P.J. Cumpson and M.P. Seah, *Surf. Interface Anal.* **25**, 430 (1997).

<sup>6</sup>H.E. Bishop, *Surf. Interface Anal.* **16**, 118 (1990).

<sup>7</sup>R. Shimizu and Z. Ding, *Rep. Prog. Phys.* **55**, 487 (1992).

<sup>8</sup>A. Jablonski and H. Ebel, *Surf. Interface Anal.* **11**, 627 (1988).

<sup>9</sup>W.H. Gries and W. Werner, *Surf. Interface Anal.* **16**, 149 (1990).

<sup>10</sup>P.J. Cumpson, *Surf. Interface Anal.* **20**, 727 (1993).

<sup>11</sup>J. M. Cowley, *Diffraction Physics* (North-Holland, Amsterdam, 1995).

<sup>12</sup>W.S.M. Werner, *Surf. Interface Anal.* **18**, 217 (1992).

<sup>13</sup>J. Bass, in *Metals: Electronic Transport Phenomena*, edited by K. H. Hellwege and J. L. Olsen, Vol. 15a of *Landolt-Börnstein, New Series, Group III* (Springer, Heidelberg, 1982).

<sup>14</sup>S.A. Lindgren, L. Walldén, J. Rundgren, and P. Westrin, *Phys. Rev. B* **29**, 576 (1984).

<sup>15</sup>G. Capart, *Surf. Sci.* **26**, 429 (1971).

<sup>16</sup>J.R. Noonan and H.L. Davis, *Vacuum* **32**, 107 (1982).

<sup>17</sup>H.L. Davis and J. R. Noonan, *Surf. Sci.* **126**, 245 (1983).

<sup>18</sup>D.L. Adams, H.B. Nielsen, and J.N. Andersen, *Surf. Sci.* **128**, 294 (1983).

<sup>19</sup>A.P. Baddorf, I.W. Lyo, E.W. Plummer, and H.L. Davis, *J. Vac. Sci. Technol. A* **5**, 782 (1987).

<sup>20</sup>Z.P. Hu, B.C. Pan, W.C. Fan, and A. Ignatiev, *Phys. Rev. B* **41**, 9692 (1990).

<sup>21</sup>J. Rundgren (unpublished).

<sup>22</sup>D.A. Liberman, D.T. Cromer, and J.T. Waber, *Comput. Phys. Commun.* **2**, 107 (1971).

<sup>23</sup>A. Rosén, D.E. Ellis, H. Adachi, and F.W. Averill, *J. Chem. Phys.* **65**, 3629 (1976).

<sup>24</sup>A. Rosén, *Advanced Quantum Chem.* **29**, 1 (1997).

<sup>25</sup>L. Hedin and B.I. Lundqvist, *J. Phys. C* **4**, 2064 (1971).

<sup>26</sup>R.E. Watson, J.F. Herbst, L. Hodges, B.I. Lundqvist, and J.W. Wilkins, *Phys. Rev. B* **13**, 1463 (1976).

<sup>27</sup>J. Neve, J. Rundgren, and P. Westrin, *J. Phys. C* **15**, 4391 (1982).

<sup>28</sup>J. Rundgren, J. Neve, and P. Westrin (unpublished).

<sup>29</sup>N. W. Ashcroft and N. D. Mermin, *Solid State Physics* (Saunders College, Philadelphia, 1976).

<sup>30</sup>J. Rundgren and A. Salwén, *J. Phys. C* **9**, 3701 (1976).

<sup>31</sup>W. Moritz, *J. Phys. C* **17**, 353 (1984).

<sup>32</sup>H. Over, U. Ketterl, W. Moritz, and G. Ertl, *Phys. Rev. B* **46**, 15 438 (1992).

<sup>33</sup>J. Philip and J. Rundgren, in *Determination of Surface Structure by LEED*, edited by P. M. Marcus and F. Jona (Plenum, New York, 1984).

<sup>34</sup>K. Heinz, *Rep. Prog. Phys.* **55**, 637 (1995).

<sup>35</sup>J.B. Pendry and D.K. Saldin, *Surf. Sci.* **145**, 33 (1984).

<sup>36</sup>B. L. Györrfy and G. M. Stocks, in *Electrons in Disordered Metals and at Metallic Surfaces*, edited by P. Phariseau, B. L. Györrfy, and L. Scheire (Plenum, New York, 1984).

<sup>37</sup>Z. Czyzewski, D.O. MacCallum, A. Romig, and D.C. Joy, *J. Appl. Phys.* **68**, 3066 (1990).

<sup>38</sup>P. R. Watson, M. A. Van Hove, and K. Hermann, *NIST Surface Structure Data Base Ver. 2.0* (National Institute of Standards and Technology, Gaithersburg, MD, 1996).